A Compact Double-Sided FSS Absorbing Wall for Decoupling 5G Antenna Arrays

Faissal Merzaki, Philippe Besnier, Mohamed Himdi, Xavier Castel, Maelle Sergolle, Thierry Levavasseur, Patrick Caldamone

A Compact Double-Sided FSS Absorbing Wall for Decoupling 5G Antenna Arrays

Faissal Merzaki, Philippe Besnier, *Senior Member, IEEE*, Mohamed Himdi, Xavier Castel, Maëlle Sergolle, Thierry Levavasseur, and Patrick Caldamone

***Abstract*—The fifth generation (5G) of mobile communications gives birth to the evolution of the base stations. They progressively include arrays of antennas in the sub-6 GHz frequency band worldwide. Moreover, 5G takes advantage of the beamforming capabilities to gain power efficiency and higher throughputs. Within this framework, achieving high decoupling performance between any pairs of antennas and compactness at the same time become a major challenge. The present paper describes an advanced solution based on the interposition of a thin and low-profile absorbing wall operating in the 3.4–3.6 GHz frequency band. The absorption is provided by a frequency selective surface whose elementary pattern size is first optimized. Then, the compact absorbing wall that associates back-to-back pieces of absorber is interposed between elements of an antenna array. Moreover, the fabrication of both antenna array and decoupling device involve lightweight and low-cost composite technology. The results show that such a compact decoupling device achieves excellent decoupling capabilities while keeping up the antenna array performance.**

***Index Terms*—Antenna decoupling, frequency selective surface (FSS) absorber, fifth generation (5G) antenna array.**

I. Introduction

PRIOR to the advent of fifth generation (5G) communications, mobile stations handling 2G, 3G, and 4G communication systems integrated all these technologies into one single device. With the forthcoming 5G technologies, the mobile station functionality needs to expand its operating frequency to host the 5G bands. Integrating those new communication systems inside a single device without modifying its size summons a major problem of electromagnetic compatibility due to the potential coupling effects between communication systems operating at various frequency bandwidths. Moreover, 5G communications support multiple-input multiple output (MIMO) transmissions to handle beamforming, as a principle for increasing data rate transmission. Coupling issues within the involved array of antennas may jeopardize the performance of MIMO transmissions that is optimum if input/output signals are uncorrelated. This article focuses on this specific issue.

The literature describes numerous strategies to decouple neighboring antennas sharing, at the moment, the same printed circuit board. We may classify these strategies in three main categories.

First, the patterning of antennas common ground plane may prevent the flowing of currents from one antenna to another. This set of solutions is based on the so-called "defected ground structure" technique. For instance, such a solution may consist in etching a thin slot into the common ground plane of an antenna array [1]–[5]. This pattern can be seen as a resonator precluding the current from flowing from one antenna to another through the ground plane. Therefore, it decreases the induced voltage difference at neighboring antennas and reduces the coupling effect, accordingly.

Second, coupling between antennas may be due to surface wave propagation into the substrate. Therefore, another method consists in positioning "electronic band gap" (EBG) structure between antennas as introduced in [6]. In this case, the EBG structure consists of a metamaterial surface (over the substrate) that prevents the propagation of surface waves through diffraction or absorption effects [7]. However, this technique suffers from its size in case of strict compactness requirements for antenna arrays. Based on the tailoring of artificial magnetic conductors (AMCs) [6] allowing reflection with a zero-phase shift, a double-sided piece of AMC surfaces was used as a vertical wall between monopole antennas [8]. This solution applies to nonplanar antennas, but remains very useful for designing low-profile and narrow band antennas [9]. However, surface waves may have significant contributions for substrate with high dielectric constant. In the case of moderate dielectric constant, this is not a predominant effect.

Third, coupling also occurs at razing incidence through electromagnetic field propagation (in the near-field zone) over the air. A lot of research works have contributed to this with various concepts of thin absorbing materials including metamaterials [10]–[12] and frequency selective surface (FSS) structures [13]–[15]. Beyond their intrinsic properties, their use as

Manuscript received May 18, 2021; revised September 1, 2021; accepted October 22, 2021. This work was supported in part by the French FUI STARCOM Project, in part the European Union through the European Regional Development Fund, in part by the Ministry of Higher Education and Research, in part by the Région Bretagne, in part by the Départements d'Ille-et-Vilaine and des Côtes d'Armor, and in part by Saint-Brieuc Armor Agglomération, through the CPER projects 2015-2020 MATECOM and SOPHIE. *(Corresponding author: Faissal Merzaki.)*

Faissal Merzaki, Philippe Besnier, Mohamed Himdi, and Xavier Castel are with the CNRS, INSA Rennes, University of Rennes, F-35000 Rennes, France (e-mail: faissal.merzaki@insa-rennes.fr; philippe.besnier@insa-rennes.fr; mohamed.himdi@univ-rennes1.fr; xavier.castel@univ-rennes1.fr).

Maëlle Sergolle is with the INSA Rennes, CNRS, University of Rennes, F-22004 Saint-Brieuc, France, and also with the Naval Group, F-44020 Bouguenais, France (e-mail: maelle.sergolle@naval-group.com).

Thierry Levavasseur and Patrick Caldamone are with the Séribase Industrie, F-53200 Chateau-Gontier, France (e-mail: t.levavasseur@seribase.fr; p.caldamone@seribase.fr).

Color versions of one or more figures in this article are available at https://doi.org/10.1109/TEMC.2021.3129368.

Digital Object Identifier 10.1109/TEMC.2021.3129368

decoupling devices is illustrated in many applications [16]–[24]. These solutions mainly consist of implementing an absorbing structure as a wall between antennas to prevent the electromagnetic field propagation over the air and thereby to enhance the decoupling without significant modification of the antenna radiation pattern. Although these various techniques exist, they focus on decoupling high-profile antennas (such as monopoles). Only a few of them deal with the specific planar MIMO configurations for 5G applications and use suspended walls or superstrates. The solution investigated here is rather based on the design of a limited size decoupling wall for decoupling an array of patch antennas.

In this article, we present a low-cost, low-profile decoupling structure for a 5G planar antenna array, including three main new features. First, the decoupling structure is made of two back-to-back pieces of FSS absorbers forming a low-profile vertical wall with no significant impact on the antenna array performance. Second, it is fabricated using lightweight composite materials and a low-cost screen-printing process to inscribe the designed FSS pattern on an aramid sheet. Third, the proposed FSS pattern is an extension of the original idea in [25] and propose to intertwine the resistive line strips on the four sides of the pattern to reinforce couplings and lowering the periodicity of the unit cell. This pattern restricts the meandering of strip lines for outmost ones, where it is the more relevant. A preliminary analysis of the candidate FSS structure was proposed in [26] and its operation and performance are further analyzed in details. The resistive surface of the decoupling device was fabricated using a screen-printing process with a home-made ink. This is the reason why recently proposed techniques based on graphene material [27]–[31] were not considered here. These solutions are not suitable to achieve the target sheet resistance value by the screen-printing process. The decoupling device is then obtained by stacking the screen-printed sheet on a composite substrate. The overall decoupling performance is optimized from numerical simulations and results are confirmed through experiments. The rest of this article is organized as follows. Section II deals with the design of the compact narrowband absorber made of an advanced FSS unit cell. It also describes its behavior when illuminated by a plane wave under oblique incidence. Section III details the fabrication process of the decoupling device. Section IV provides experimental evidence of its intrinsic absorbing performance. In Section V, the retained FSS structure is then shaped as a vertical wall for decoupling an array of stub-loaded antennas in the 3.4–3.6 GHz frequency band. Eventually, the experimental validation of the obtained decoupling device is presented. Section VI concludes the article.

II. FSS Absorber Unit Cell Design

An FSS absorber is composed of a periodic resistive pattern lying on a dielectric substrate with an electromagnetic reflector stacked on the opposite side. The contrast between the FSS absorber input impedance and the wave impedance determines the operating frequency band in which a minimum reflection coefficient is achieved. As described in [14], absorption takes place at the neighborhood of the resonance frequency of the

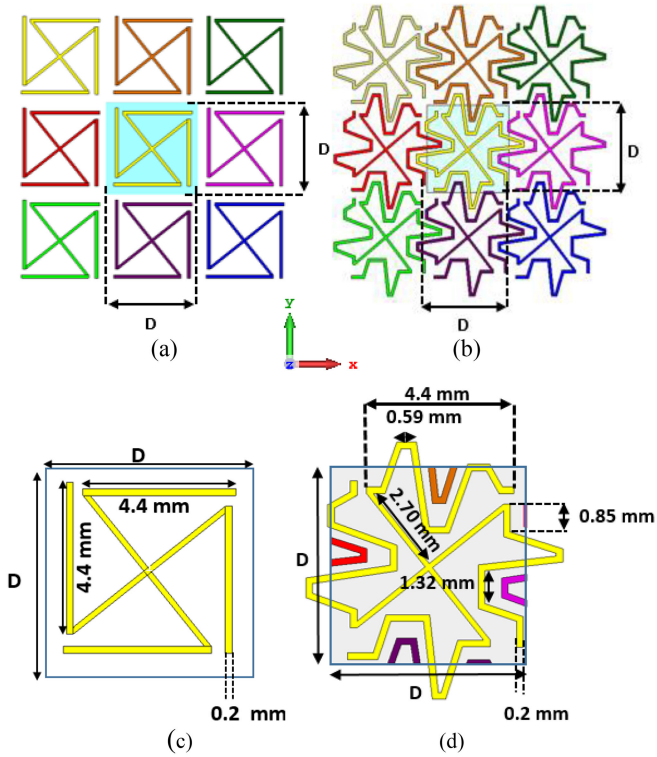

Fig. 1. (a) Periodic basic FSS design and (b) proposed FSS design ($D = 5.9$ mm). (c) Dimensions of the basic unit cell. (d) FSS unit cell.

stand-alone FSS pattern. The latter behaves as a simple resonant R, L, C circuit for a basic resistive pattern made of a patch, cross, or loop, where C and L stand for the mutual electric and magnetic coupling between adjacent cells, respectively, and R accounts for a resistance related to the pattern resistivity. The impedance at the FSS pattern interface is composed of the parallel association of the patterned surface and the impedance brought back from the grounded dielectric substrate [14]. Adjusting the thickness (which remains thin with regard to the wavelength), it is possible to obtain a narrowband absorber or a broadband absorber for a thicker dielectric. The maximum absorption occurs when the imaginary part of the two parallel impedances are opposite, the resistivity being adjusted to fulfill matching conditions.

The proposed FSS absorber was developed considering the original idea in [25] that consisted in interdigitating adjacent cells. In this article, authors demonstrated that such pattern lowered the resonance frequency, increasing mutual coupling between contiguous cells. This suggests that intertwining neighboring cells should favors an increase of mutual coupling. While keeping the same approach, we therefore propose an evolution of the pattern, intertwining the resistive line strips on its four sides to reinforce couplings and lowering the periodicity of the unit cell. This pattern restricts the meandering of strip lines for outmost ones, where it is the more relevant. Furthermore, it was developed both to fulfill width resolution limitation (about 100 μm) and the range of attainable sheet resistance with home-made inks. Our design started from the elementary pattern in Fig. 1(a) showing a freestanding FSS structure called ZZ_{inv} (in series association of Z-shaped and inverted Z-shaped

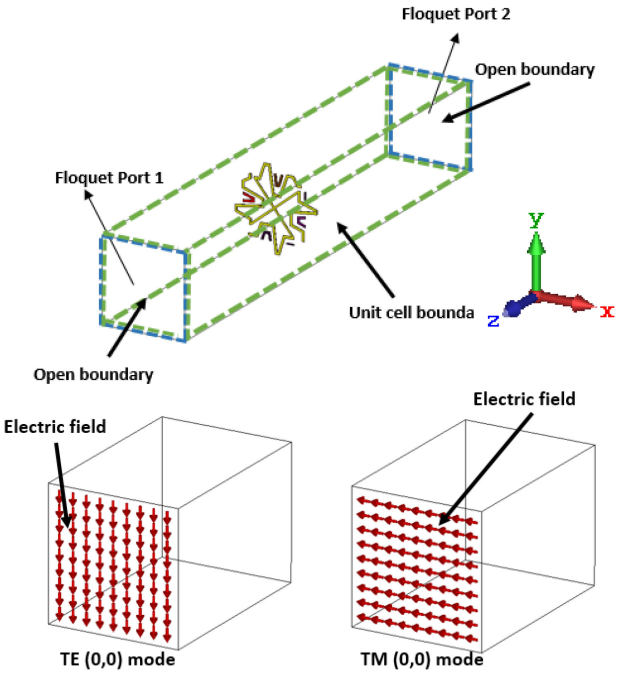

Fig. 2. Physical representation of the TZZ_{inv} unit cell free-standing simulation and the excitation modes of the plane wave.

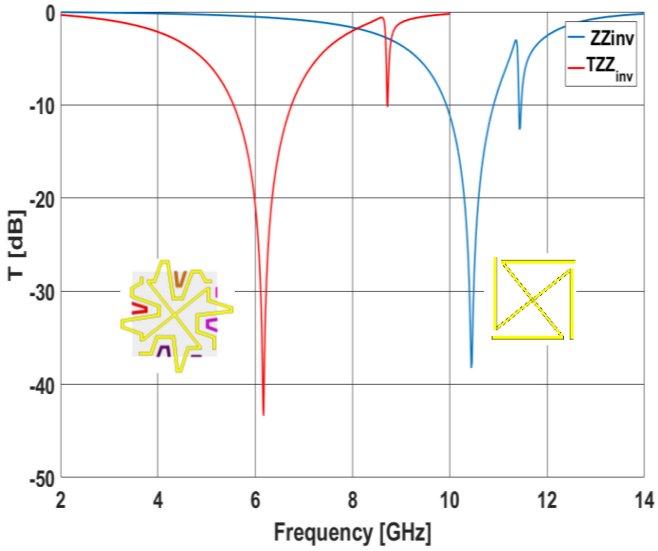

Fig. 3. Simulated transmission coefficient T of the free-standing ZZ_{inv} and TZZ_{inv} patterns versus frequency.

resistive ribbons) as developed in [25]. Our proposed TZZ_{inv} (in series association of transformed Z-shaped and inverted Z-shaped resistive ribbons), structure initially presented in [26], is then presented in Fig. 1(b). It is first evaluated through a free-standing FSS simulation of an infinitely periodic and metallic (copper) FSS sheet in air in comparison with the initial ZZ_{inv} pattern. Reducing the resonance frequency of an FSS structure leads to an intrinsic shift of the absorption frequency band toward lower frequencies when this resonant structure is transformed to FSS absorber, which is highlighted in the article. Note that both structures have the same periodicity ($D = 5.9$ mm). The geometry of the unit cell for the initial ZZ_{inv} pattern and for the TZZ_{inv} pattern is detailed in Fig. 1(c) and (d), respectively.

Fig. 2 shows the physical view of the boundary conditions that has been ensured to simulate the FSS transmission coefficient of the free-standing pattern for both cases using the frequency solver of CST Microwave Studio. Simulations were carried out using two Floquet ports positioned on both sides of the z-axis. The boundary conditions are set at the unit cell level for x-, y-axis (shown in the green dashed rectangular parallelepiped). So, the structure is expanded periodically and infinitely in the xy plane. An open boundary condition is set along z-axis (blue squares) allowing incident wave to propagate through z-axis with minimum reflection before and after reaching the infinite structure. The FSS structure is illuminated by a normal incident plane wave source either in the transverse electric (TE) or in the transverse magnetic (TM) mode and located at the Floquet port 1. The transmission coefficient is therefore the transmitted power from the Floquet port 1 toward the Floquet port 2 located on the other side of the structure. Simulations of the transmission coefficient provide a better picture of the resonating nature of FSS patterns. The results of such simulations of both patterns are reported in Fig. 3.

The resonance frequency of the ZZ_{inv} pattern, which is characterized by a null transmission coefficient, equals 10.44 GHz whereas the TZZ_{inv} pattern exhibits a similar resonating behavior at a much lower frequency (6.17 GHz). Therefore, the decrease of the resonance frequency utterly comes from an increase of the mutual capacitance and inductance.

With the aim of developing a compact FSS absorber with an operating frequency centered at 3.5 GHz with a 200 MHz-bandwidth, a parametric study of the dielectric permittivity is carried out to achieve the absorption peak at 3.5 GHz. Afterward, the sheet resistance optimization of the TZZ_{inv} pattern is carried out to achieve the maximum absorption. The parametric study is performed with a 4 mm-thick dielectric substrate ($\lambda/21.5$ at 3.5 GHz).

Simulations are carried out by setting an unit cell boundary in the xy plane (at the four sides of the green dashed rectangular parallelepiped), and because of the presence of a reflector at the bottom of the absorber, a perfect electric boundary condition is set to feature a perfect ground plane (highlighted in red dash square, Fig. 4) in order to minimize the calculation time. Therefore, a single Floquet port is used as shown also in Fig. 4. The structure is illuminated by an incident plane wave source located at the Floquet port1 and the reflection coefficient is calculated at this port location.

Fig. 5 displays the TZZ_{inv} simulations of 36 μm-thick copper ribbons ($\sigma = 5.96 \times 10^7$ S/m) printed on a grounded 4 mm-thick dielectric substrate. When the dielectric permittivity ε_r increases, the absorption peak decreases smoothly toward low frequency. The absorption peak sets at 3.58 GHz with $\varepsilon_r = 3$ and at 3.46 GHz with $\varepsilon_r = 4$. Thus, to achieve the peak absorption at 3.5 GHz, the dielectric permittivity value could be expected to range between 3 and 4.

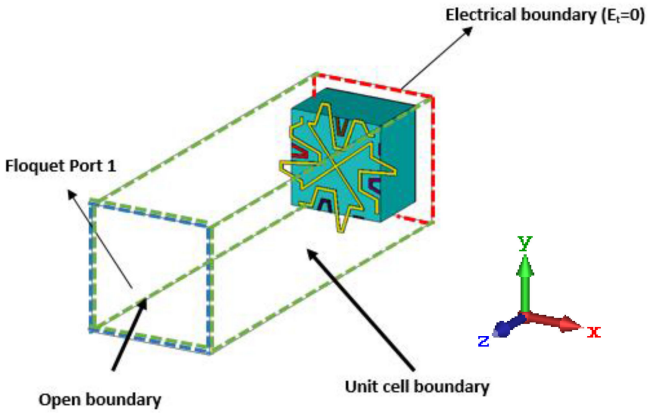

Fig. 4. Physical representation of the TZZ_{inv} absorber.

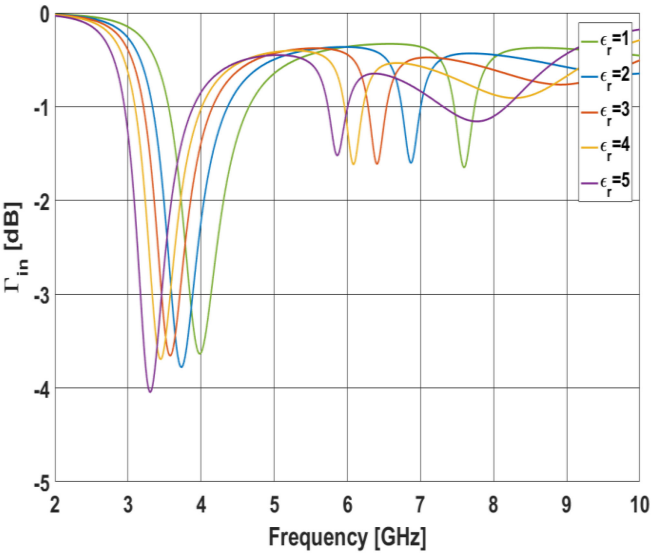

Fig. 5. Simulated reflection coefficient vs. dielectric permittivity values of a copper TZZ_{inv} pattern printed on a 4 mm-thick dielectric substrate.

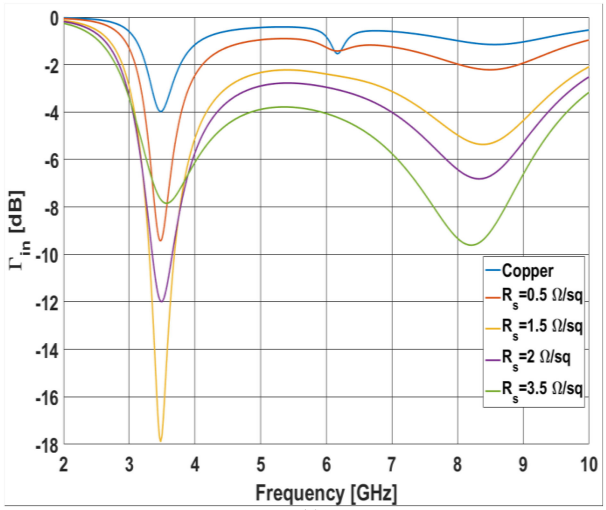

(a)

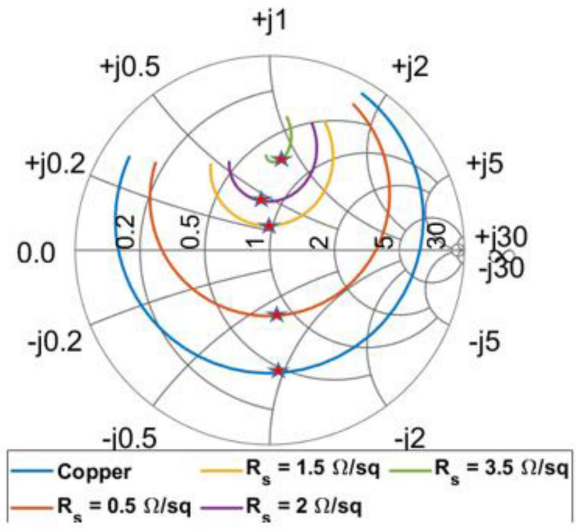

(b)

Fig. 6. Simulated reflection coefficient vs. sheet resistance values of conductive and resistive TZZ_{inv} patterns printed on a 4 mm-thick dielectric substrate with (a) $\varepsilon_r = 3.5$. Magnitude [dB] versus frequency and (b) Smith chart from 3 GHz to 4 GHz (b). The red star is located at 3.5 GHz.

To get the maximum absorption peak at 3.5 GHz, the dielectric permittivity value was set at 3.5 and new numerical simulations were performed by varying the sheet resistance value of the ribbons (see Fig. 6). With ribbons made of metallic conductor (copper with a sheet resistance $R_s = 0.0005\ \Omega$/sq), the absorption peak reaches -3.98 dB at 3.47 GHz. When the sheet resistance value increases, the peak absorption level increases as the Ohmic loss in the TZZ_{inv} pattern increases and the input impedance of the overall absorber matches with the free space impedance. This matching reaches its maximum at $R_s = 1.5\ \Omega$/sq and the related absorption level achieves -18 dB at 3.47 GHz. Beyond 1.5 Ω/sq, the input impedance unmatched the free space impedance and the absorption peak level decreases.

Based on the previous TZZ_{inv} parametric studies, a compact absorbing FSS structure, called $ATZZ_{inv}$ was developed to operate in the 3.4–3.6 GHz frequency band. This absorber is characterized by a periodicity of only $D = 5.9$ mm ($\lambda/14.5$ at 3.5 GHz). The optimized sheet resistance of the ribbons is equal to 1.5 Ω/sq. The simulated substrate is a composite material made of glass fiber tissue and polyester resin. It is characterized by a dielectric permittivity $\varepsilon_r = 3.7$, a loss tangent $\tan\delta = 0.0094$ and a thickness $t = 4$ mm.

Fig. 7 provides an illustration of the simulated absorber whereas Fig. 8 shows the related simulated reflection coefficient at normal incidence over the 3–4 GHz frequency range. As a result, the absorption coefficient is better than -10 dB from 3.3 to 3.65 GHz. To assess the performance of the $ATZZ_{inv}$ FSS absorber, its simulated reflection coefficient was compared with that of the AZZ_{inv} FSS absorber in the same configuration, i.e., using the same sheet resistance value of the resistive ribbons ($R_s = 1.5\ \Omega$/sq) and the same dielectric substrate. At normal incidence, the AZZ_{inv} cell based absorbing material reaches its maximum absorption at 6.5 GHz against 3.5 GHz for the $ATTZ_{inv}$ absorber. The gain in size is therefore of about 46%. Note that these simulations aim at comparing the position of

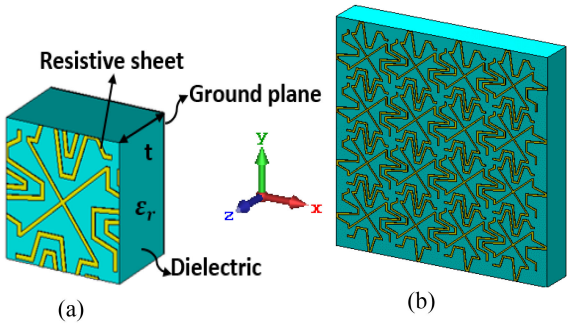

Fig. 7. (a) $\mathbf{ATZZ_{inv}}$ unit cell pattern and (b) $\mathbf{ATZZ_{inv}}$ FSS absorber periodic pattern.

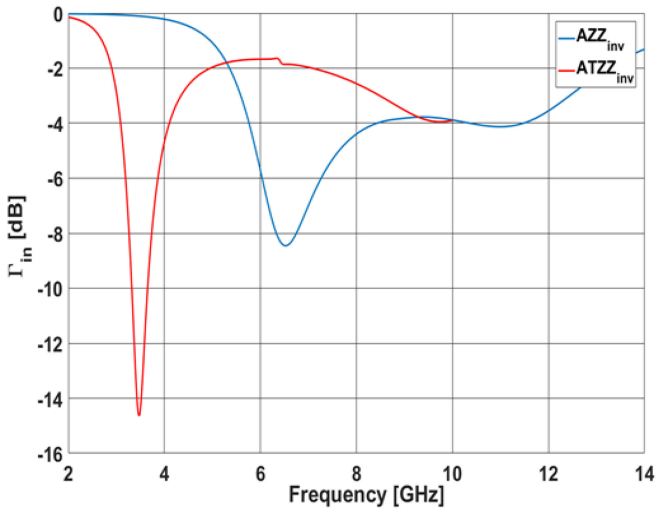

Fig. 8. Simulated reflection coefficient comparison vs. frequency of the $\mathrm{AZZ_{inv}}$ and $\mathbf{ATZZ_{inv}}$ absorbers at normal incidence.

the frequency absorption peak and not the absorption level. To compare the absorption levels of both structures, a sheet resistance optimization of the $\mathrm{AZZ_{inv}}$ resistive ribbons needs to be performed.

Fig. 9 illustrates the power loss density at 2 and 3.5 GHz of the $\mathrm{ATZZ_{inv}}$ FSS absorber under the TE mode excitation. Power loss is mainly concentrated at upper and lower borders of contiguous FSS cells at 3.5 GHz compared with that at 2 GHz, which confirms the absorption effect at 3.5 GHz for the TE mode (electric field aligned with the y-axis). Under TM mode excitation, power loss is concentrated at the left and right borders of the unit cells (not shown here).

Such $\mathrm{ATZZ_{inv}}$ absorber will be used in Section V to decouple antennas exposed to EM waves impinging at incidence angles different from normal incidence. Simulations are achieved using the boundary conditions of Fig. 4. By controlling a CST software predefined variable, the propagating wave direction is tuned to any required incident angle. Therefore, Fig. 10 illustrates the simulated reflection coefficient of the $\mathrm{ATZZ_{inv}}$ FSS structure under four incident angles θ_i in the TE mode (similar results, not shown here, are obtained in the TM mode). The absorption performance decreases under oblique incidence angle with an

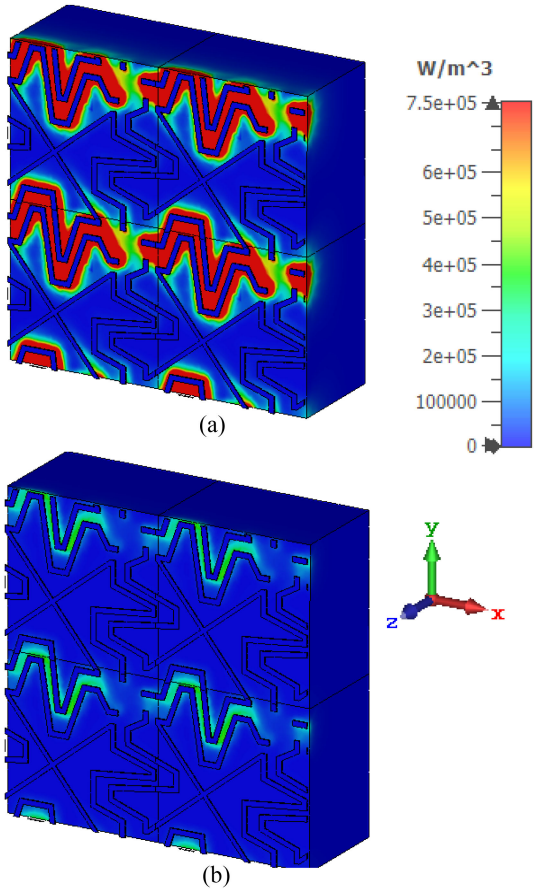

Fig. 9. Power loss density of the $\mathrm{ATZZ_{inv}}$ FSS absorber at (a) 3.5 GHz and (b) 2 GHz under TE mode excitation.

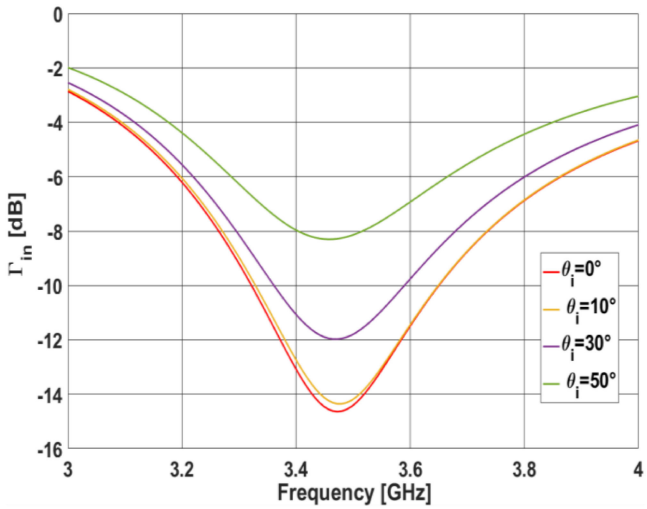

Fig. 10. Simulated reflection coefficient vs. frequency of the $\mathrm{ATZZ_{inv}}$ FSS absorber under various incident angles θ_i.

absorption coefficient lower than -10 dB on a more restricted frequency range, but not anymore at $\theta_i = 50°$.

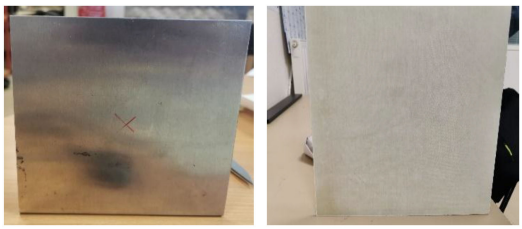

(a) (b)

Fig. 11. (a) Metallic ground plane and (b) dielectric composite substrate.

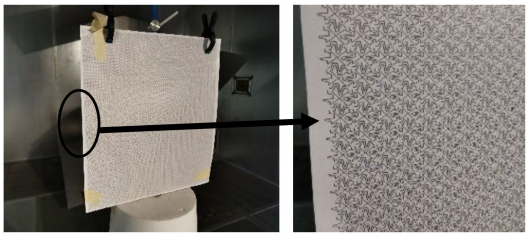

Fig. 12. Global view and detail of the $ATZZ_{inv}$ FSS absorber printed on a 100 μm-thick aramid sheet.

III. Fabrication Process

The dielectric substrate is made of a fiber-reinforced matrix. The FSS pattern is printed on a dielectric sheet and stuck on the top face of the dielectric substrate.

On the one hand, the 4 mm-thick fabricated substrate (S2-glass fiber tissue infused with polyester resin) was characterized at microwaves. Its dielectric permittivity $\varepsilon_r = 3.7 \pm 0.5$ and loss tangent $\tan\delta = 9.4\times10^{-3} \pm 0.5\times10^{-3}$ from 100 MHz to 1 GHz were retrieved from impedance measurements [32]. The dielectric composite substrate is then associated with a 2 mm-thick aluminum plate on its back-side (see Fig. 11).

On the other hand, the FSS pattern was printed using a screen-printing process based on a home-made ink (53.1% PF410 silver ink and 46.9% 6017SS carbon ink by weight) to get the required sheet resistance value of 1.5 Ω/sq (see Fig. 12). It is worth noting that the process resolution achieves an accuracy of 100 μm. The resistive FSS was patterned on a 100 µm-thick aramid sheet. The size of the aramid sheet, of the dielectric substrate and of the metallic plate equals 35 cm × 35 cm.

The absorbing performance of the fabricated absorber was measured using estimation of the radar cross section computed from *S*-parameters.

IV. Measurement Method and Experimental Results

Absorbing efficiency measurement is based on the retrieval of the radar cross-section (RCS) in an anechoic chamber (see Fig. 13). It is made possible through the retrieval of the ballistic backscattered wave from the target and by analyzing the scattering *S*-parameter as measured from *TX* and *RX* antennas in a quasi-monostatic configuration. The antennas were placed at a distance of 4 m from the sample. Identification of the target, considered as a point source scatter, was achieved using time gating of the inverse Fourier transform of the spectral response.

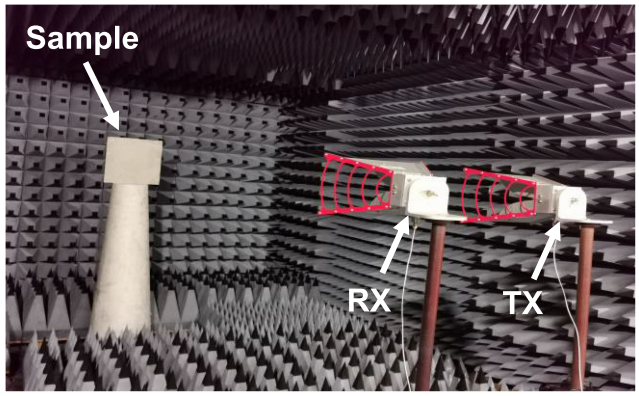

Fig. 13. RCS measurement setup.

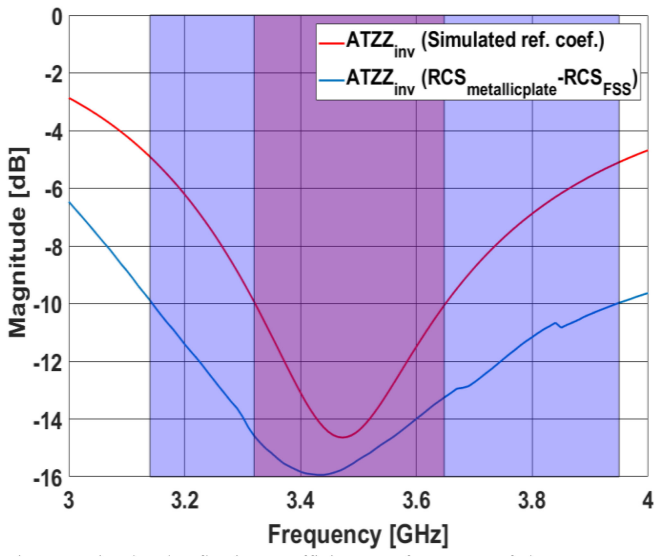

Fig. 14. Simulated reflection coefficient vs. frequency of the $ATZZ_{inv}$ FSS absorber compared with the difference between the RCS measurement of the metallic plate and that of the $ATZZ_{inv}$ FSS absorber placed in front of the metallic plate. Colored frames feature the simulated and measured absorption bandwidths (reflection coefficient lower than −10 dB).

The measurement of the absorbing FSS structure followed a two-step procedure. The first step consisted in measuring the RCS of the metallic plate. The second step consisted in measuring the FSS placed in front of such metallic plate. The contrast of RCS provides the absorbing performance of the FSS device, at normal incidence of the electromagnetic quasi-plane wave.

Fig. 14 shows the comparison of the simulated reflection coefficient of the two-dimensional infinite FSS absorber and the ratio between the RCS of the 35 cm × 35 cm FSS absorber and of the 35 cm × 35 cm metallic plate. This difference in the logarithmic scale is analogous to the magnitude of a reflection coefficient that can be directly compared with numerical simulation. The experimental result indicates that the realized absorbing FSS owns a maximum level of absorption at 3.43 GHz against 3.50 GHz for numerical simulation. The absorption bandwidth at −10 dB is 3.15–3.94 GHz, which remains wider than the simulated one (3.32–3.62 GHz). This difference is probably due to the difficulty in controlling the sheet resistance of the resistive

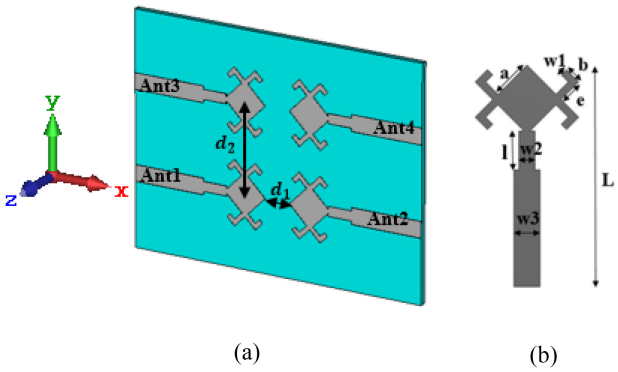

Fig. 15. (a) Representation of the four-elements antenna array and (b) detailed view of a single antenna.

TABLE I
PHYSICAL DIMENSIONS OF THE SLP ANTENNA ARRAY

Parameter	Values (mm)
d_1	16.0
d_2	57.0
a	16.5
b	7.00
w_1	3.00
w_2	6.35
w_3	10.5
l	15.5
L	89.0
e	10.0

ribbons all over the 35 cm × 35 cm sample size. Furthermore, the simulation is performed using periodic boundary conditions that do not take into account the finite size of the fabricated sample. As a reminder, TZZ_{inv} absorption is sensitive to the ribbon sheet resistance value (see Fig. 6), a little variation in R_s value modifying the behavior of the overall FSS structure.

V. APPLICATION TO ANTENNA DECOUPLING

A. Stub Loaded Patch (SLP) Antenna Array

Utility of the FSS absorber for the reduction of the mutual coupling between antenna elements of an array is now assessed. An array of four patch antennas operating in the 5G 3.4–3.6 GHz frequency band is therefore considered. Each patch owns a set of four stubs attached symmetrically at the two opposite corners of their square patch. Hence, they are named SLP antennas. This four elements array is presented in Fig. 15. In the following, the four antennas are called Ant1, Ant2, Ant3, and Ant4 according to their labeling in Fig. 15(a). The physical dimensions of the antenna array are given in Table I. Its fabrication uses a composite dielectric substrate with a permittivity $\varepsilon_r = 2.4$, a loss tangent of 0.0047 and a thickness $t = 4$ mm. Note that the spacing between antennas is only $d_1 = 16$ mm from edge to edge [see Fig. 15(a)].

Fig. 16 shows the magnitude of the reflection coefficient S_{11} of Ant1 and the magnitude of scattering parameters from Ant1 to all other antennas, namely Ant2, Ant3, and Ant4. From

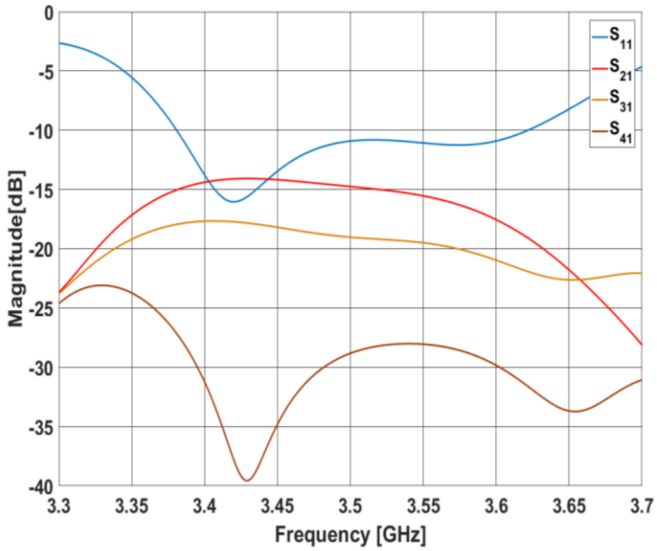

Fig. 16. Simulated *S*-parameters versus frequency of Ant1.

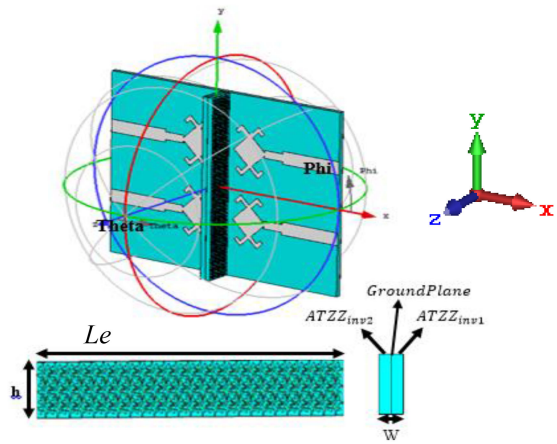

Fig. 17. Four-elements antenna array with the decoupling wall made of two $ATZZ_{inv}$ FSS absorbers.

the S_{11} measurement, the operating frequency of the array lies between 3.38 and 3.62 GHz, S_{11} being less than −10 dB over this frequency range. In that operating frequency band, the scattering coefficients to Ant2 (S_{21}) and Ant4 (S_{41}), i.e., in the direction of the *E*-plane cut of the radiation pattern, vary from −15 to −19 dB and from −25 to −40 dB, respectively. In the direction of the *H*-plane cut, the coupling coefficient S_{31} varies from −18 to −22 dB. Specifications in terms of 5G MIMO antennas require that the coupling between each antenna remains at least lower than −20 dB. Therefore, to enhance our MIMO antenna system, the interposition of the proposed $ATZZ_{inv}$ FSS absorber is investigated to preclude the radiation coupling.

B. Decoupling Wall Absorber and Height Optimization

The decoupling device consists of the back-to-back association of two FSS absorbers of type $ATZZ_{inv}$. They form a vertical wall between antennas to be decoupled. Fig. 17 shows the insertion of such decoupling wall in the *E*-plane of the

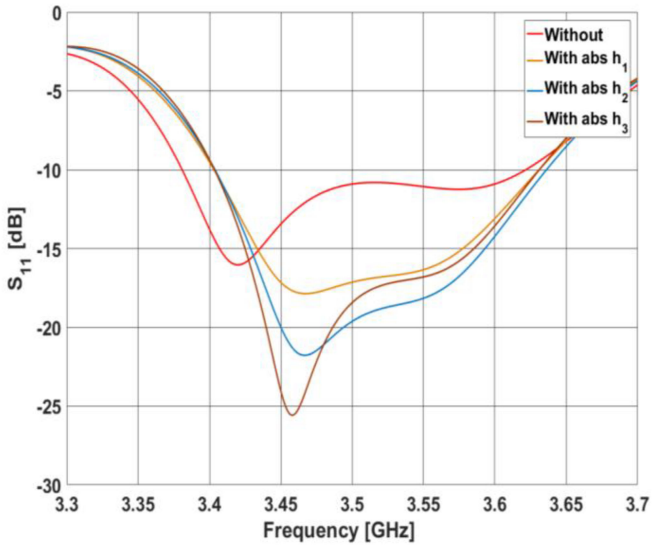

Fig. 18. Simulated S_{11} parameter versus frequency of Ant1 for various heights of decoupling wall ($h_1 = 12$ mm; $h_2 = 18$ mm; $h_3 = 24$ mm).

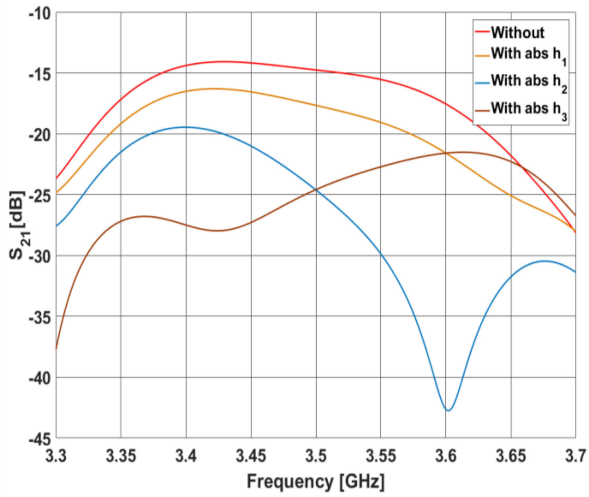

Fig. 19. Simulated $\boldsymbol{S}_{21}$ parameter versus frequency of Ant1 for various heights of decoupling wall ($h_1 = 12$ mm; $h_2 = 18$ mm; $h_3 = 24$ mm).

TABLE II
HEIGHT OF THE FSS DECOUPLING ABSORBER

Configuration	Height of the absorber (mm)
h_1 (two-rows)	12
h_2 (three-rows)	18
h_3 (four-rows)	24

antenna array where the coupling is significant. The thickness of the interposed device equals $W = 8$ mm, i.e., twice the thickness of a single absorber. Its length *Le* equals 150 mm. Its height was optimized to achieve a suitable tradeoff between significant decoupling achievements on the one hand and preservation of antenna radiation patterns on the other hand. Note that the separation from the decoupling device to each antenna is only 4 mm from edge to edge.

The optimization of the absorber height was achieved by varying the number of rows of the FSS design. The absorber performance was evaluated through the antenna input impedance, coupling rate, and radiation pattern impacts.

Fig. 18 shows the reflection coefficient of Ant1 for a two-rows (h_1), a three-rows (h_2) and a four-rows (h_3) configurations of unit cells. Table II gives the corresponding wall height values. Whatever the absorber configuration, the operating frequency of the array is slightly shifted to 3.4–3.63 GHz. Insertion of the wall absorber therefore enhances the matching performance, specifically above 3.45 GHz. More importantly, Fig. 19 highlights that the magnitude of the scattering parameter between Ant1 and Ant2 (S_{21}) is lower than -20 dB over the frequency range where Ant1 is matched for $h_2 = 18$ mm and $h_3 = 24$ mm. A very significant decoupling effect occurs beyond 3.5 GHz. At height h_3 , the decoupling wall operates as expected from 3.4 to 3.5 GHz where the decoupling is significantly improved compared with h_2. Beyond the latter frequency, the coupling coefficient remains below -20 dB but the performance is much lower than that with height h_2. We assume that diffraction by the edges of the absorbing wall causes this deterioration.

To ensure that decoupling reduction at height $h_2$is lying on the absorption mechanism and not on diffraction effect, we performed additional numerical simulations removing either the FSS sheets or both sheets and dielectric substrates. Fig. 20 illustrates the transmission coefficients S_{21} and S_{31} where only the metallic plate remains, with addition of the substrates and finally with the complete back-to-back FSS decoupling wall. As far as S_{21} is concerned, the FSS sheets allow a remarkable reduction of the transmission coefficient from 3.5 to 3.6 GHz compared with those of the metallic plate and dielectric substrate. This leads us to confirm that decoupling beyond 3.5 GHz is indeed due to the absorption effect. Moreover, the decoupling effect with regard to Ant3 is also demonstrated. The presence of the absorber wall shows a remarkable reduction of the coupling by an average of -4 dB from 3.4 to 3.5 GHz, once the FSS sheets are added onto the grounded dielectric substrates.

The height h_2 has been selected here as the optimized height of the FSS absorber, because of its performance achieved in the 3.5–3.6 GHz frequency band. Furthermore, its decoupling effect is linked to electromagnetic absorption and not to diffraction effect that may be detrimental to antenna radiation pattern. All transmission *S*-parameters from Ant1 to any other antennas are displayed in Fig. 21, with and without the h_2-high decoupling wall. It appears that transmission coefficients remain below -20 dB for all parameters in the 3.43–3.6 GHz frequency range.

Fig. 22 highlights the current distribution generated by Ant1 with and without the h_2-high FSS decoupling wall at 3.6 GHz. The current distribution of Ant1 is weakly modified by the presence of the absorber wall while current distributions induced in Ant 2 and Ant4 are significantly reduced.

C. Fabrication of the SLP Antennas Array

The four-elements antenna array was fabricated from a homemade 4 mm-thick composite laminate material. The dielectric

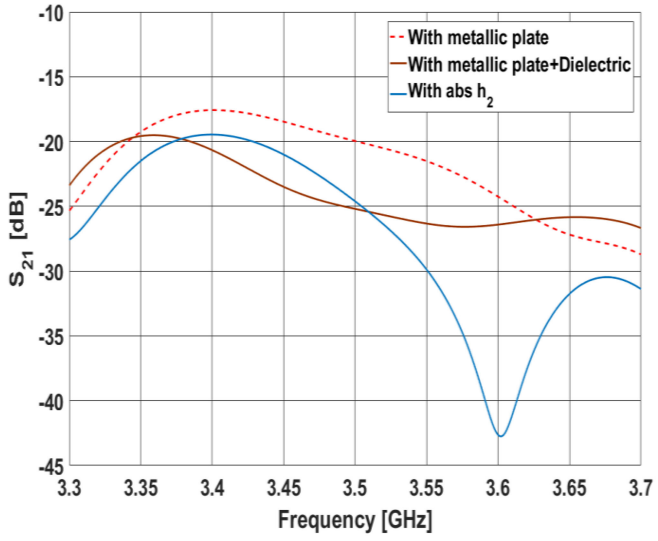

(a)

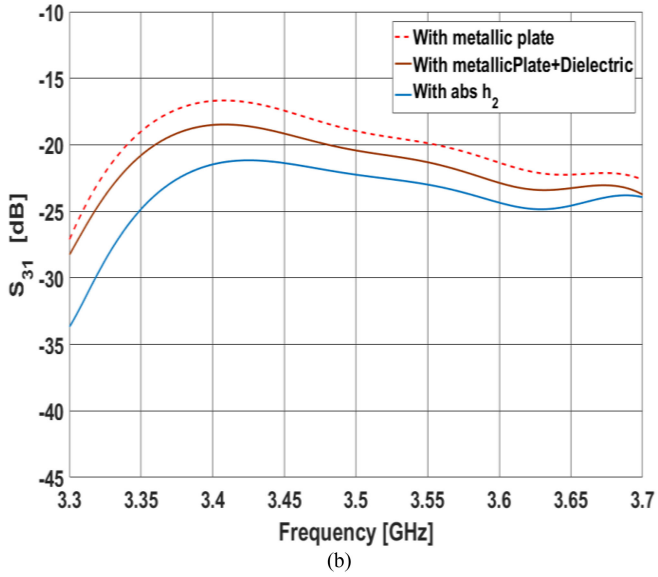

(b)

Fig. 20. (a) Simulated S_{21} and (b) S_{31} parameters versus frequency with the metallic plate; with the metallic plate and the dielectric substrate; and with the complete FSS decoupling wall of height h_2.

substrate consists of Innegra fabric (woven polypropylene fibers, namely a 340 g/m^2 taffeta) infused with polyester resin. It exhibits a dielectric permittivity $\varepsilon_r = 2.4 \pm 0.4$ and a loss tangent $\tan\delta = 4.7\times10^{-3} \pm 0.5\times10^{-3}$ from 100 MHz to 1 GHz, values retrieved from impedance measurements. The conductive layers placed on both sides of the dielectric substrate are made of a 293 g/m^2 0.12 mm-thick copper woven fabric exhibiting a sheet resistance value $R_s = 6\times10^{-4}$ Ω/sq (measured from a standard 4-probe setup).

The composite laminate material was fabricated by the vacuum infusion process. Five plies of Innegra fabric were stacked between two plies of copper fabric (single ground plane for the bottom; radiating elements and related feeding lines for the top). The whole was located on a glass slab. Placed under vacuum (−0.6 bar) with a plastic bag as shown in Fig. 23, the copper and

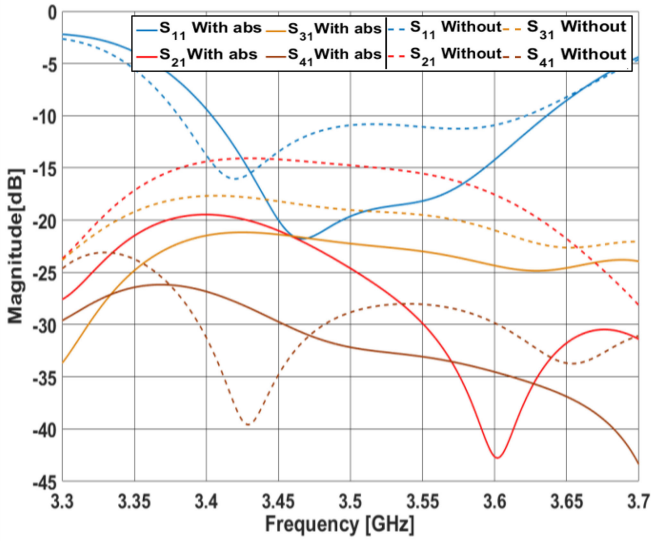

Fig. 21. Simulated *S*-parameters versus frequency with and without the h_2-high FSS decoupling wall.

Innegra fabrics were infused jointly with a liquid polyester resin (with 2% by weight of catalyst). After the resin polymerization at room temperature for 24 h followed by a postcure step at 40°C for 16 h, the composite laminate material, made of the dielectric substrate sandwiched between the two copper fabrics, was suitable for release. Afterward a three-axis machine was used to make the four microstrip antennas by subtractive method. The top copper fabric was therefore machined under 0.20 mm deep, removing out the unnecessary conductive layer. As shown in Fig. 24, the fabricated antenna array was characterized using a two-port VNA. Nonconnected antennas are left open.

Fig. 25 shows that the addition of the h_2-high FSS decoupling wall does not alter the antenna array bandwidth (3.28–3.58 GHz) although a frequency shift is recorded with respect to numerical simulations.

On the one hand, the transmission coefficient from Ant1 to Ant2 (S_{21}) is mostly above −20 dB (−17 dB at maximum) over that frequency range if no decoupling device is present. On the other hand, the insertion of the h_2-high FSS decoupling wall provides a significant decoupling of at least −21 dB and up to −25 dB over the same frequency range. The absence of a much higher decoupling performance as predicted at 3.6 GHz by numerical simulation (see Fig. 19) is supposedly due to the presence of the connectors at the onset of the antenna feeding lines. The decoupling performance toward Ant3 is enhanced of −4 dB from 3.5 to 3.55 GHz. Similarly, it is improved of about −4 dB at 3.4 GHz and −8 dB at 3.5 GHz toward Ant4.

In order to investigate the role of the connectors, *E*-plane radiation pattern of Ant1 was simulated and measured without the presence of the FSS decoupling wall at two frequencies: 3.5 and 3.6 GHz (see Fig. 26). At 3.5 GHz, the measured radiation pattern exhibits a minimum level at 30° of -10 dB, i.e., 6 dB below the simulated directivity in the same direction. This difference reaches −14 dB with regard to numerical simulation at

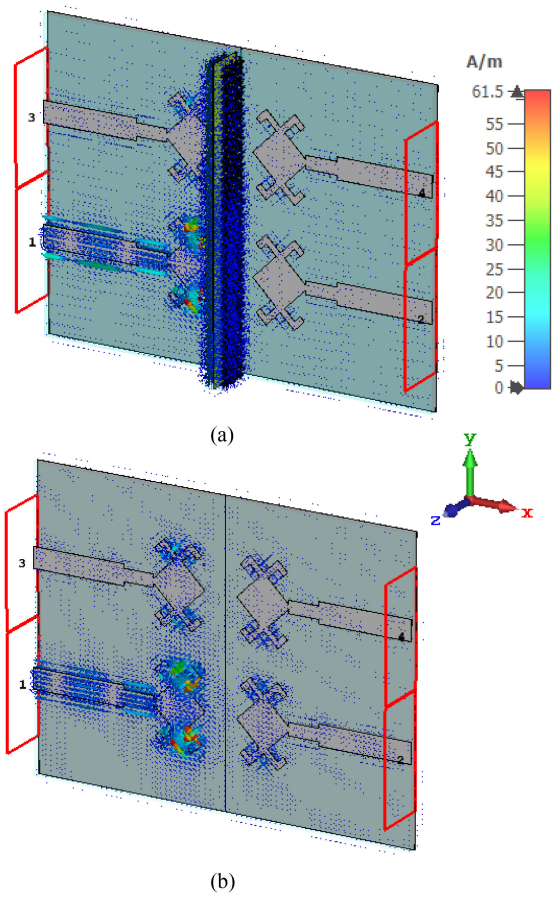

Fig. 22. Surface current distribution of the h_2-high FSS decoupling wall at 3.6 GHz of Ant1 (a) with and (b) without absorber at 3.6 GHz.

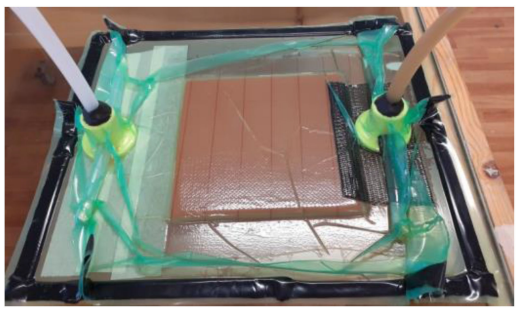

Fig. 23. Vacuum infusion mounting to fabricate the home-made SLP antenna array.

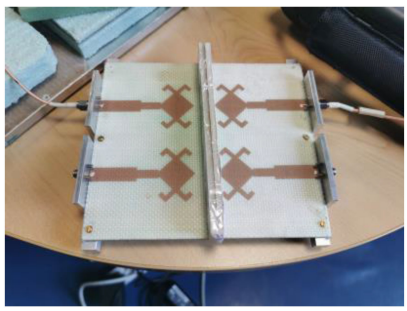

Fig. 24. Home-made four-elements SLP antenna array with the FSS decoupling wall standing in *E*-plane.

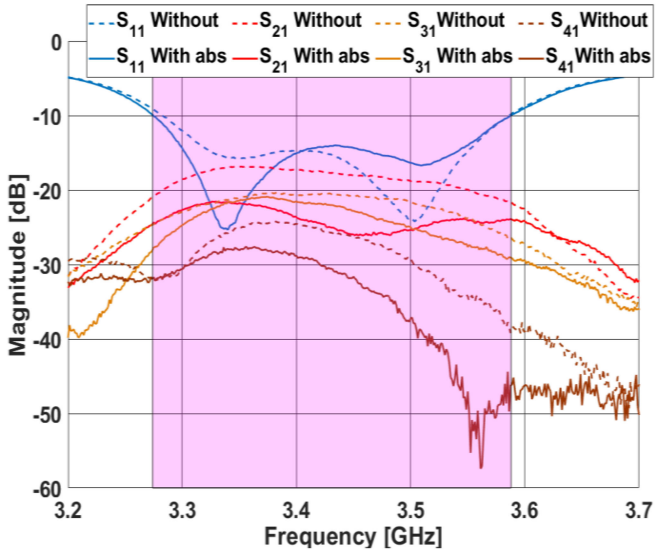

Fig. 25. Measurement of the *S*-parameters from Ant1, with and without the h_2-high FSS decoupling wall.

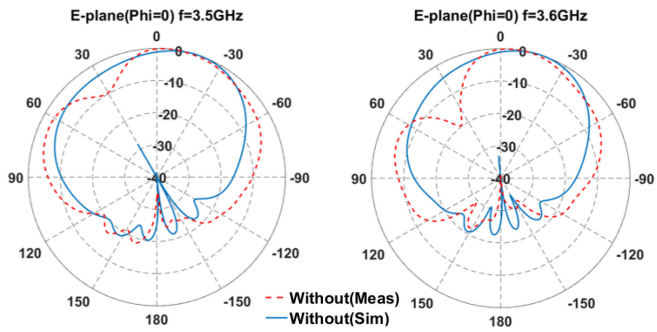

Fig. 26. Simulation and measurement of Ant1 radiation patterns in *E*-plane at 3.5 and 3.6 GHz without the FSS decoupling wall.

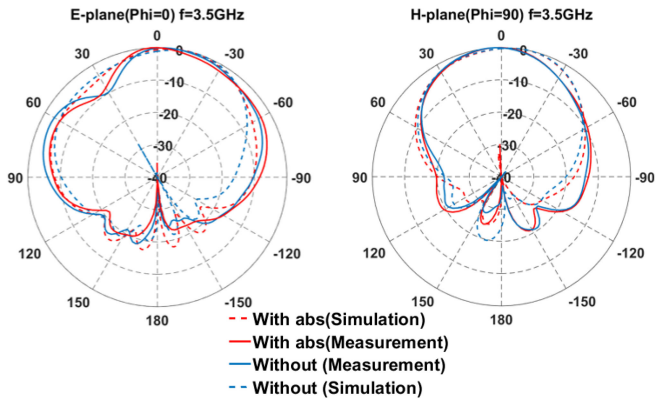

Fig. 27. Simulation and measurement of Ant1 radiation patterns in *E*-plane and *H*-plane at 3.5 GHz, with and without the h_2-high FSS decoupling wall.

3.6 GHz. Furthermore, we have confirmed from another simulation (not shown here) that the presence of comparable metal pieces causes this radiation pattern alteration.

Fig. 27 presents the *E*-plane and *H*-plane Ant1 radiation patterns at 3.5 GHz retrieved from simulations and measurements, with and without the h_2-high FSS decoupling wall. The

presence of the absorber causes a slight shift of the main lobe direction (4°) which is fully acceptable. Meanwhile, the *H*-plane radiation pattern has not been impacted by the presence of such decoupling wall. We may therefore conclude that this simple, compact and low-cost decoupling device enables to fulfill mutual decoupling requirements below −20 dB and, at the same time, fully preserves the antenna array performance.

VI. Conclusion

Mutual coupling between antennas of 5G base station is a critical issue with regard to beamforming capabilities. In this article, we have designed, fabricated, and investigated a specific composite absorber for mutual decoupling of an antenna array. This solution is based on a compact back-to-back FSS absorber wall of 8 mm-width and 18 mm-high above the planar antenna array.

The pattern of the unit-cell array was first optimized to reduce its size with regard to the wavelength, using intertwining cells. This led to the fabrication of an FSS absorber associating a composite laminate substrate fabricated by vacuum infusion process and a screen-printed sheet with an optimized sheet resistance value ($R_s = 1.5\ \Omega$/sq). Intrinsic performance of the FSS absorber has been confirmed from experiments.

Then, the obtained absorbing structure was configured as a back-to-back FSS to form a decoupling wall for preventing mutual coupling of a planar SLP antenna array. The back-to-back FSS wall size was optimized through numerical simulations. Experimental validations are then performed to assess the mutual coupling reduction into the antenna array.

The achieved antenna array and decoupling device prototypes highlight the decoupling performance. Mutual coupling between antennas remains below −20 dB over the targeted frequency range (3.4–3.6 GHz), fulfilling this stringent requirement for so close antennas. At the same time, radiation pattern measurements also confirm that the proposed decoupling device do not introduced any significant alteration.

We believe that such a solution may be extended to various designs of antenna arrays in the frame of future deployment of 5G (and beyond) to reduce mutual coupling in base stations for MIMO antenna arrays.

Acknowledgment

The authors would like to thanks J. Sol (IETR) for his technical assistance for microwave measurements and K. Desmars (SERIBASE Industrie) for his assistance in screen-printing process.

References

[1] Z. Zakaria, N. A. Shairi, R. Sulaiman, and W. Y. Sam, "Design of reconfigurable defected ground structure (DGS) for UWB application," in *Proc. IEEE Asia-Pac. Conf. Appl. Comp. Electromagn. Soc.*, Dec. 2012, pp. 195–198, doi: 10.1109/APACE.2012.6457659.

[2] D. Gao, Z. X. Cao, S. D. Fu, X. Quan, and P. Chen, "A novel slot-array defected ground structure for decoupling microstrip antenna array," *IEEE Trans. Antennas Propag.*, vol. 68, no. 10, pp. 7027–7038, Oct. 2020, doi: 10.1109/TAP.2020.2992881.

[3] K. Wei, J. Y. Li, L. Wang, Z. J. Xing, and R. Xu, "Mutual coupling reduction by novel fractal defected ground structure bandgap filter," *IEEE Trans. Antennas Propag.*, vol. 64, no. 10, pp. 4328–4335, Oct. 2016, doi: 10.1109/TAP.2016.2591058.

[4] K. Wei, J. Li, L. Wang, Z. Xing, and R. Xu, "S-shaped periodic defected ground structures to reduce microstrip antenna array mutual coupling," *Electron. Lett.*, vol. 52, no. 15, pp. 1288–1290, Jul. 2016, doi: 10.1049/el.2016.0667.

[5] A. Habashi, J. Nourinia, and C. Ghobadi, "Mutual coupling reduction between very closely spaced patch antennas using low-profile folded split-ring resonators (FSRRs)," *IEEE Antennas Wireless Propag. Lett.*, vol. 10, pp. 862–865, Aug. 2011, doi: 10.1109/LAWP.2011.2165931.

[6] G. Goussetis, A. P. Feresidis, and J. C. Vardaxoglou, "Tailoring the AMC and EBG characteristics of periodic metallic arrays printed on grounded dielectric substrate," *IEEE Trans. Antennas Propag.*, vol. 54, no. 1, pp. 82–89, Jan. 2006, doi: 10.1109/TAP.2005.861575.

[7] H. S. Farahani, M. Veysi, M. Kamyab, and A. Tadjalli, "Mutual coupling reduction in patch antenna arrays using a UC-EBG superstrate," *IEEE Antennas Wireless Propag. Lett.*, vol. 9, pp. 57–59, Feb. 2010, doi: 10.1109/LAWP.2010.2042565.

[8] Z. Bayraktar, M. Gregory, and D. H. Werner, "Composite planar double-sided AMC surfaces for MIMO applications," in *Proc. IEEE Int. Symp. Antennas Propag. Soc.,* Jun. 2009, pp. 1–4, doi: 10.1109/APS.2009.5171816.

[9] A. P. Feresidis, G. Goussetis, S. Wang, and J. C. Vardaxoglou, "Artificial magnetic conductor surfaces and their application to low-profile high-gain planar antennas," *IEEE Trans. Antennas Propag.*, vol. 53, no. 1, pp. 209–215, Jan. 2005, doi: 10.1109/TAP.2004.840528.

[10] N. I. Landy, S. Sajuyigbe, J. J. Mock, D. R. Smith, and W. J. Padilla, "Perfect metamaterial absorber," *Phys. Rev. Lett.*, vol. 100, no. 20, May 2008, Art. no. 207402, doi: 10.1103/PhysRevLett.100.207402.

[11] N. Engheta, "Thin absorbing screens using metamaterial surfaces," in *Proc. IEEE Int. Symp. Antennas Propag. Soc.*, Jun. 2002, pp. 392–395, doi: 10.1109/APS.2002.1016106.

[12] K. P. Kaur, T. Upadhyaya, and M. Palandoken, "Ultrathin wideband polarization independent compact metamaterial microwave absorber," in *Proc. Int. Conf. Radioelektronika*, Apr. 2018, pp. 1–6, doi: 10.1109/RADIOELEK.2018.8376395.

[13] I. S. Syed, Y. Ranga, L. Matekovits, K. P. Esselle, and S. G. Hay, "A single-layer frequency selective surface for ultrawideband electromagnetic shielding," *IEEE Trans. Electromagn. Compat.*, vol. 56, no. 6, pp. 1404–1411, Dec. 2014, doi: 10.1109/TEMC.2014.2316288.

[14] F. Costa, A. Monorchio, and G. Manara, "Analysis and design of ultra thin electromagnetic absorbers comprising resistively loaded high impedance surfaces," *IEEE Trans. Antennas Propag.*, vol. 58, no. 5, pp. 1551–1558, May 2010, doi: 10.1109/TAP.2010.2044329.

[15] F. Costa, A. Monorchio, and G. Manara, "An equivalent circuit model of frequency selective surfaces embedded within dielectric layers," in *Proc. IEEE Int. Symp. Antennas Propag. Soc.*, Jun. 2009, pp. 1–4, doi: 10.1109/APS.2009.5171774.

[16] Z. Wang, L. Zhao, Y. Cai, S. Zheng, and Y. Yin, "A meta-surface antenna array decoupling (MAAD) method for mutual coupling reduction in a MIMO antenna system," *Sci. Rep.*, vol. 8, no. 1, Feb. 2018, Art. no. 3152, doi: 10.1038/s41598-018-21619-z.

[17] M. Ghaderi and N. C. Karmakar, "Frequency selective surface for reducing mutual coupling in antenna arrays," in *Proc. Asia-Pac. Microw. Conf.*, Dec. 2011, pp. 1877–1880.

[18] X. L. Li, G. M. Yang, and Y. Q. Jin, "Isolation enhancement of wideband vehicular antenna array using fractal decoupling structure," *IEEE Antennas Wireless Propag. Lett.*, vol. 18, no. 9, pp. 1799–1803, Sep. 2019, doi: 10.1109/LAWP.2019.2930365.

[19] R. Karimian, A. Kesavan, M. Nedil, and T. A. Denidni, "Low-mutual-coupling 60-GHz MIMO antenna system with frequency selective surface wall," *IEEE Antennas Wireless Propag. Lett.*, vol. 16, pp. 373–376, Jun. 2016, doi: 10.1109/LAWP.2016.2578179.

[20] B. Zhang, J. M. Jornet, I. F. Akyildiz, and Z. P. Wu, "Mutual coupling reduction for ultra-dense multi-band plasmonic nano-antenna arrays using graphene-based frequency selective surface," *IEEE Access*, vol. 7, pp. 33214–33225, Mar. 2019, doi: 10.1109/ACCESS.2019.2903493.

[21] H. Qi, L. Liu, X. Yin, H. Zhao, and W. J. Kulesza, "Mutual coupling suppression between two closely spaced microstrip antennas with an asymmetrical coplanar strip wall," *IEEE Antennas Wireless Propag. Lett.*, vol. 15, pp. 191–194, Jun. 2015, doi: 10.1109/LAWP.2015.2437995.

[22] X. M. Yan, X. G. Liu, X. Y. Zhou, and T. J. Cui, "Reduction of mutual coupling between closely packed patch antennas using waveguided metamaterials," *IEEE Antennas Wireless Propag. Lett.*, vol. 11, pp. 389–391, Apr. 2012, doi: 10.1109/LAWP.2012.2193111.

[23] M. Akbari, H. A. Ghalyon, M. Farahani, A.-R. Sebak, and T. A. Denidni, "Spatially decoupling of CP antennas based on FSS for 30-GHz MIMO systems," *IEEE Access*, vol. 5, pp. 6527–6537, Apr. 2017, doi: 10.1109/ACCESS.2017.2693342.

[24] Y. J. Song and K. Sarabandi, "Suppression of the mutual coupling between two adjacent miniaturized antennas utilizing printed resonant circuits," in *Proc. IEEE Int. Symp. Antennas Propag. Soc.,* Jun. 2009, pp. 1–4, doi: 10.1109/APS.2009.5171523.

[25] S. Barbagallo, A. Monorchio, and G. Manara, "Small periodicity FSS screens with enhanced bandwidth performance," *Electron. Lett.*, vol. 42, no. 7, pp. 382–384, Mar. 2006, doi: 10.1049/el:20060329.

[26] F. Merzaki *et al.*, "A compact absorbing FSS structure for antenna decoupling in the 5G 3.5GHz band," in *Proc. IEEE Int. Symp. Electromagn. Compat.*, Sep. 2020, pp. 1–6, doi: 10.1109/EMCEUROPE48519.2020.9245649.

[27] A. Rinaldi, A. Proietti, A. Tamburrano, and M. S. Sarto, "Graphene-coated honeycomb for broadband lightweight absorbers," *IEEE Trans. Electron. Compat.*, vol. 60, no. 5, pp. 1454–1462, Oct. 2018, doi: 10.1109/TEMC.2017.2775660.

[28] B. Xu, C. Gu, Z. Li, L. Liu, and Z. Niu, "A novel absorber with tunable bandwidth based on graphene," *IEEE Antennas Wireless Propag. Lett.*, vol. 13, pp. 822–825, Apr. 2014, doi: 10.1109/LAWP.2014.2319083.

[29] M. Qu, T. Chang, G. Guo, and S. Li, "Design of graphene-based dual-polarized switchable rasorber/absorber at terahertz," *IEEE Access*, vol. 8, pp. 127220–127225, Jul. 2020, doi: 10.1109/ACCESS.2020.3008417.

[30] C. Huang, J. Song, C. Ji, J. Yang, and X. Luo, "Simultaneous control of absorbing frequency and amplitude using graphene capacitor and active frequency-selective surface," *IEEE Trans. Antennas Propag.*, vol. 69, no. 3, pp. 1793–1798, Mar. 2021, doi: 10.1109/TAP.2020.3011115.

[31] M. Geng, Z. Liu, W. Wu, H. Chen, B. Wu, and W. Lu, "A dynamically tunable microwave absorber based on graphene," *IEEE Trans. Antennas Propag.*, vol. 68, no. 6, pp. 4706–4713, Jun. 2020, doi: 10.1109/TAP.2020.2972646.

[32] M. Sergolle, X. Castel, M. Himdi, P. Besnier, and P. Parneix, "Structural composite laminate materials with low dielectric loss: Theoretical model towards dielectric characterization," *J. Composites C, Open Acess,* vol. 3, Nov. 2020, Art. no. 100050, doi: 10.1016/j.jcomc.2020.100050.

Faissal Merzaki received the master's degree in electrical and electronic engineering in 2018 from Rennes1 University, Rennes, France, where he is currently working toward the Ph.D. degrees in electrical engineering.

His research interests include electromagnetic absorbers, specifically for the 5G and V\UHF application.

Philippe Besnier (Senior Member, IEEE) received the Diplôme d'ingénieur degree from École Universitaire D'ingénieurs de Lillle, Lille, France, in 1990 and the Ph. D. degree in electronics from the University of Lille, Lille, France, in 1993.

Following a one-year period, he was an Assistant Scientist with the EMC division, ONERA, Meudon, France. He was with the Laboratory of Radio-Propagation and Electronics, University of Lille, as a Researcher (chargé de recherche) with the Centre National de la Recherche Scientifique (CNRS), from 1994 to 1997. From 1997 to 2002, he was the Director of Centre d'Etudes et de Recherches en Protection Electromagnétique: a non-for-profit organization for research, expertise and training in EMC and related activities, based in Laval, France. He also co-Founded TEKCEM in 1998, a small business company specialized in turn-key systems for EMC measurements. Back to CNRS in 2002, he has been since then with the Institut d'Electronique et des Technologies du numéRique, Rennes, France. He was appointed as a CNRS Senior Researcher (Directeur de recherche au CNRS) in 2013. He was co-head of the "antennas and microwave devices" research Department of the IETR, between 2012 and 2016. He headed the WAVES (electromagnetic waves in complex media) team during the first semester of 2017. Since July 2017, he has been the Deputy Director of the IETR. His research interests include interference analysis on cable harnesses (including electromagnetic topology), theory and application of reverberation chambers, shielding and absorbing techniques, near-field probing and uncertainty quantification in EMC modeling.

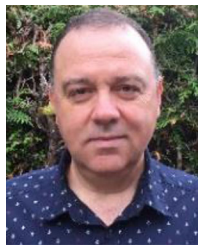

Mohamed Himdi received the Ph.D. degree in signal processing and telecommunications from the University of Rennes 1, Rennes, France, in 1990.

Since 2003, he has been a Professor with the University of Rennes 1, and the Head of the High Frequency and Antenna Department until 2013, of IETR. He has authored or co-authored 147 journal papers and more than 280 papers in conference proceedings. He has also co-authored ten book chapters. He holds 46 patents. His research activities concern passive and active millimeter-wave antennas. His research also includes development of new architectures of antenna arrays, and new 3-D antenna technologies. He was Laureate of the 2-D National Competition for the Creation of Enterprises in Innovative Technologies in 2000 (Ministry of Industry and Education).

Dr. Himdi was the recipient of the JEC-AWARD, Paris, France, on Pure composite material antenna embedded into a motorhome roof for the Digital Terrestrial Television reception, in March 2015, and also the Innovation Trophy 2021 from University of Rennes 1.

Xavier Castel received the Ph.D. degree in material science from the University of Rennes 1, Rennes, France, in 1997.

From 1999 to 2016, he was an Associate Professor with the Technological Institute of Saint-Brieuc, University of Rennes 1, Saint-Brieuc, France, and a Researcher with the Institute of Electronics and Telecommunications of Rennes, University of Rennes 1, where he was nominated as a Full Professor, in 2017. He is currently the Co-Head of the Functional Materials Team with the Department of Antennas and Microwave Devices. He has authored and co-authored about 60 international papers, more than 235 conference presentations, and holds 22 patents. His main research interests include the elaboration of advanced materials (transparent and conducting materials, superconductors, semiconductors, composite materials) for microwave applications, their physical-chemical characterizations (electrical, optical, structural, microstructural, thermal, mechanical properties, etc.) and the fabrication of the related microwave devices and antennas (by photolithographic technique, wet-etching process, lift-off process and laser micro-etching).

Dr. Castel is a recipient and co-recipient of eight scientific awards.

Maëlle Sergolle received the Ph.D. degree in materials and electronic from the University of Rennes 1, Rennes, France, in 2020.

She iscurrently a Research Engineer in composite materials for electromagnetic applications. Her thesis work concerned the use of composite materials to implement antenna and electromagnetic devices embedded into structural panels. Since 2020, she has been with Naval Group, Paris, France.

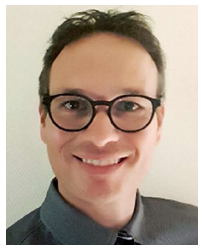

Patrick Caldamone received the DUT Physical measurement in 1997, Marketing control of scientific equipment in 1999, and the Master degree in instrumentation and sensors and industrial communication from Fac St. Charles de Marseille, Marseille, France, in 2000.

At first, he traded international measuring equipment with Algeria Then after a stay abroad (England/Ireland). He was with the Séribase Industrie. During ten years, he developed the commercial activity in France and in Europe. Then, he joined the design office in 2015 in research, development and innovations.

Thierry Levavasseur, photograph and biography not available at the time of publication.